nature photonics

SUPPLEMENTARY INFORMATION

DOI: 10.1038/NPHOTON.2017.128

In the format provided by the authors and unedited.

Depolarization signatures map gold nanorods within biological tissue

Norman Lippok,[a,b] Martin Villiger,[a,b] Alexandre Albanese,[c,d] Eelco F. J. Meijer,[a,e] Kwanghun Chung,[d,f–h] Timothy P. Padera,[a,e] Sangeeta N. Bhatia,[c,d,i] and Brett E. Bouma,[a,b,d]

[a] *Harvard Medical School, Boston, MA, USA*
[b] *Wellman Center for Photomedicine, Massachusetts General Hospital, Boston, MA, USA*
[c] *Koch Institute for Integrative Cancer Research, Massachusetts Institute of Technology, Cambridge, MA, USA*
[d] *Institute for Medical Engineering and Science, Massachusetts Institute of Technology, Cambridge, MA, USA*
[e] *Edwin L. Steele Laboratories, Department of Radiation Oncology, Massachusetts General Hospital, Boston, MA, USA*
[f] *Picower Institute for Learning and Memory, Massachusetts Institute of Technology, Cambridge, MA, USA*
[g] *Department of Chemical Engineering, Massachusetts Institute of Technology, Cambridge, MA, USA*
[h] *Department of Brain and Cognitive Sciences, Massachusetts Institute of Technology, Cambridge, MA, USA*
[i] *Department of Electrical Engineering & Computer Science, Massachusetts Institute of Technology, Cambridge, MA, USA*

This article contains supplementary information to the manuscript entitled "Depolarization signatures map gold nanorods within biological tissue". Here, we validate the diattenuation response of gold nanorods (GNRs) with numerical simulations and experimentally and detail how to derive definitive depolarization as a GNR signature from coherent measurements. We compare GNR depolarization with fluorescence and two photon luminescence, illustrate the implication of noise and nanoparticle aggregation and develop an analytic model to determine absolute GNR concentration.

I. GOLD NANOROD DIATTENUATION

Due to GNRs having a high aspect ratio and a size much smaller than optical wavelengths, they permit electrons to move and oscillate more readily in response to incident radiation oriented along their longitudinal axis. We conducted simulations using the finite–difference time–domain method (FDTD) to compute the differential scattering cross-section of individual GNRs, obtained from the cross–sections corresponding to horizontally and vertically polarized probing radiation, $\sigma_{H,V}$. **Supplementary Figure S1a** shows the simulated differential scattering cross–section for various GNR aspect ratios. The normalized differential scattering cross-section approaches 1 in the vicinity of a GNRs longitudinal resonance, supporting the argument of a nearly perfect diattenuator.

We also measured the diattenuation, μ_{exp}, of GNR suspensions and intralipid (IL) experimentally. The GNRs had a size of 10 x 81 nm with a longitudinal resonance at 1200 nm. The insets in **Supplementary Figure S1b** unveil a mean diattenuation of 0 for both GNRs and IL. This is expected for IL, which consists of spherical particles that do not diattenuate or alter the polarization of singly-backscattered light. In the case of GNRs, this result can be appreciated when considering that the size of a single GNR is small compared to the coherence volume. The diattenuation seen in the inset of **Supplementary Figure S1b** is the combined diattenuation of numerous GNRs ($\sim$ 2.4 x 10^8 particles per microliter, for 400 pM). Depending on the number of GNRs and their relative orientation, they can add up constructively to result in a highly diattenuating pure state, or cancel each other, leading to a pure state with low diattenuation, causing a high variance in the measured diattenuation values. In order to obtain an estimate of the diattenuation of a single GNR, we treated the experimental measurement of an ensemble of particles as an inverse problem. A numerical simulation (**Methods**) was conducted that modelled scatterers with a set diattenuation coefficient, μ_{set}, and random diattenuation axis orientation. The simulated variance of diattenuation, $V(\mu)$, is shown by the black, solid line in **Supplementary Figure S1b**. The green and purple points correspond to our measurements for the diattenuation variance of GNRs [$V(\mu_{\mathrm{exp}}) = 0.33$] and IL [$V(\mu_{\mathrm{exp}}) = 0.02$], respectively. The experimental diattenuation variance of GNRs points to a high diattenuation coefficient of 0.75 for a single GNR using this simple model. At high diattenuation, a small change in diattenuation variance corresponds to a large change in the diattenuation coefficient. Because a small diattenuation bias cannot be precluded in our instrumentation, a diattenuation coefficient larger than 0.75 is plausible. Indeed, an uncertainty of 0.02 in the measurement of the diattenuation variance yields a diattenuation coefficient of up to 0.92. Our observation supports the argument that strong diattenuation of uncontrolled and randomly orientated GNRs is a mechanism of polarization entropy. It is important to note that a single GNR or the coherent superposition of several GNRs act as a diattenuator, while the incoherent superposition of these pure states across an ensemble of GNRs leads to depolarization.

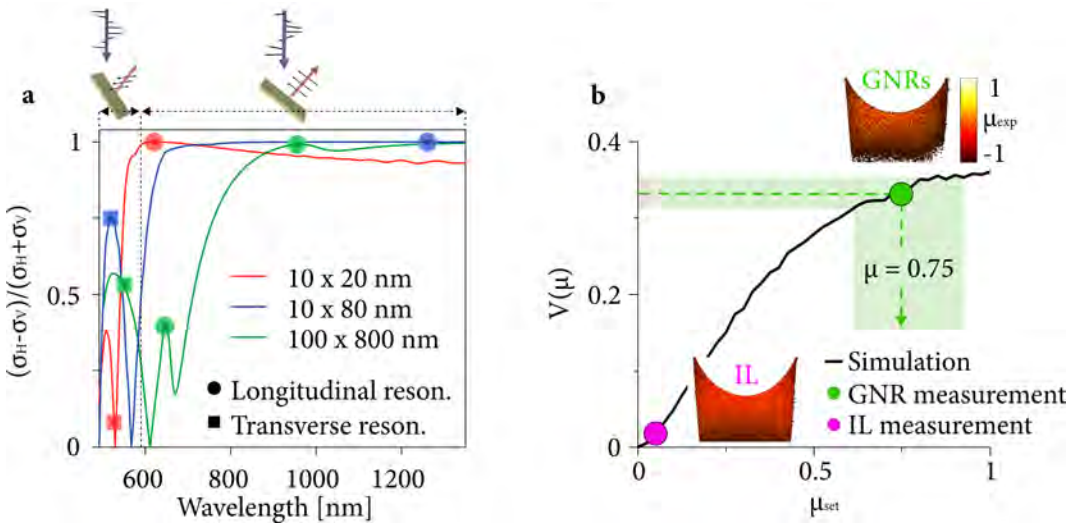

Figure S1 | Diattenuation of gold nanorods. a, Comparison of the far-field differential scattering cross-section of GNRs of different aspect ratios. The longitudinal and transverse resonances are highlighted. **b**, The insets show the experimental diattenuation coefficient, μ_{exp}, of IL and GNRs. The mean diattenuation is zero for both targets. The variance of diattenuation, however, is negligible for IL and high for GNRs due to random diattenuating axes orientation of individual GNRs per measurement volume. The black curve shows a numerical simulation of the variance of diattenuation as a function of set diattenuation, μ_{set}, from coherent particle backscatter signals. The purple and green point corresponds to our measurements of the variance of diattenuation from the inset for IL, $V(\mu_{\mathrm{exp}}) = 0.02$, and GNRs, $V(\mu_{\mathrm{exp}}) = 0.33$, projecting a single GNR diattenuation of 0.75 with a standard deviation depicted by the green area.

II. THEORY

Coherently gated, interferometric detection provides a statistical ensemble of pure states, $|\Psi\rangle$, with probability p that are combined into mixed states corresponding to an incoherent density operator

$$\boldsymbol{\rho} = \sum_{\mathrm{s}} p_{\mathrm{s}} |\Psi_{\mathrm{s}}\rangle\langle\Psi_{\mathrm{s}}| \equiv \sum_{\mathrm{j}} \sum_{\mathrm{l}} \hat{\boldsymbol{\rho}}_{\mathrm{jl}} \,, \tag{S1}$$

where index s is a running variable and j, l indexes coordinates in space, while $\hat{\boldsymbol{\rho}} = |\Psi\rangle\langle\Psi|$ is a density matrix describing a pure state. This most general form of a density operator describes system entropy, S, after Eigendecomposition, $\boldsymbol{\rho} = \sum_{\mathrm{j}=1,2} \upsilon_{\mathrm{j}} |\mathrm{j}\rangle\langle\mathrm{j}|$, where υ_{j} are eigenvalues and $|\mathrm{j}\rangle$ eigenvectors,

$$S(\boldsymbol{\rho}) = -\sum_{\mathrm{j}=1,2} \upsilon'_{\mathrm{j}} \log_2(\upsilon'_{\mathrm{j}}) \,. \tag{S2}$$

Here, $\upsilon'_{\mathrm{j}} = \upsilon_{\mathrm{j}} / \sum \upsilon$ are the relative probabilities of each principle component with $0 \leq \upsilon'_{\mathrm{j}} \leq 1$ and a logarithm to base 2 so that $0 \leq S \leq 1$. The density matrix of a mixed state on the left hand side in Equation S1 is equivalent to the coherency matrix and formally connects entropy with the degree-of-polarization (DOP). This is readily shown by extracting the eigenvalues of $\boldsymbol{\rho}$ in traditional form, $0 = |\boldsymbol{\rho} - \upsilon \boldsymbol{I}| = \upsilon^2 - \upsilon(J_{\mathrm{xx}} + J_{\mathrm{yy}}) + J_{\mathrm{xx}} J_{\mathrm{yy}} - J_{\mathrm{xy}} J_{\mathrm{yx}}$, where $|\cdot|$ is the determinant, $\boldsymbol{I}$ is the identity matrix and J_{mn} are matrix elements of $\boldsymbol{\rho}$. Eventually we arrive at

$$\begin{aligned} \upsilon_{1,2} &= \frac{1}{2}\left(1 \pm \frac{\sqrt{{J_{\mathrm{xx}}}^2 + {J_{\mathrm{yy}}}^2 - 2J_{\mathrm{xx}}J_{\mathrm{yy}} + 4J_{\mathrm{xy}}J_{\mathrm{yx}}}}{J_{\mathrm{xx}} + J_{\mathrm{yy}}}\right) \\ &= \frac{1}{2}(1 \pm \mathrm{DOP}) \,. \end{aligned} \tag{S3}$$

Indeed, entropy, decoherence and depolarization ($\Delta = 1 - \mathrm{DOP}$) are expressed by probabilities of pure states as is well known from quantum statistical mechanics.

In depolarization metrology it is crucial to account for the spatial margins of the density operator. The dimensions of speckle are characteristic for source coherence and resolution and are a useful reference for depolarization measurements. For an increasing number of observables (speckle, pure states) in the operator, depolarization increases as is seen by the decrease in Stokes vector magnitude for GNRs in **Figure 1c** (green). For the non-depolarizing target, the point of gravity of the Stokes vector cloud is askew from the sphere origin (non-uniform distribution) with an augmented probability for consistent pure states, as clearly seen in **Figure 1c** (purple). In **Supplementary Figure S2**, $\Delta = 1 - \mathrm{DOP}$ and depolarization power[1] (D) are shown as a function of the number of observables. Δ does not reach 1 but converges to approximately 0.93, slightly below the theoretical curve for a total depolarizer. This is attributed to a remaining diattenuation bias in our measurements as well as the possibility that the GNRs may not be perfect diattenuators, i.e. GNRs also scatter at the transverse plane.

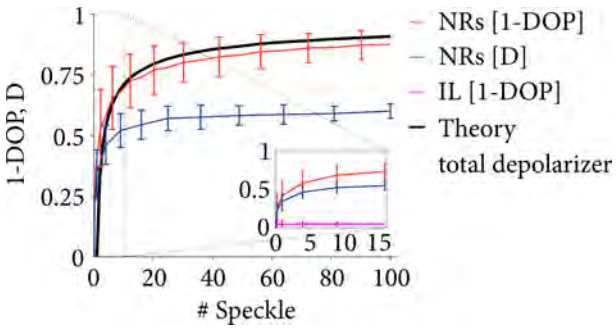

Figure S2 | Instantaneous depolarization. A depolarization measurement depends on the number of observables used in the density operator. For measurement consistency, an optimized density operator expresses nearly total depolarization for noise (total depolarizer).

Ideally, the density operator should yield nearly full depolarization for noise, which is completely depolarized.

Definitive Depolarization

DOP characterizes the depolarization of a propagating field, which can vary depending on an object's orientation (diattenuation, retardation and depolarization axis) and is only a relative measure of depolarization. The full Müller matrix offers depolarization power (index) (D) of the object itself rather than the electric field and is independent of orientation and incident polarization state, and thus an absolute measure of depolarization. From a set of basis vectors (two orthogonal Jones vectors) incident at the object simultaneously, we recast the Jones matrix, $\boldsymbol{\Psi}$ (see **Methods**, **Experimental set-up**), that is transformed into a Müller-Jones matrix, $\hat{\boldsymbol{M}}$. Similar to the density operator forming a mixed state, a distribution of Jones matrices or Müller-Jones matrices is represented by a Müller matrix[2,3],

$$\boldsymbol{M} = \sum_{\mathrm{s}} p_{\mathrm{s}} \hat{\boldsymbol{M}}_{\mathrm{s}} \equiv \sum_{\mathrm{j}} \sum_{\mathrm{l}} \hat{\boldsymbol{M}}_{\mathrm{jl}}\,, \tag{S4}$$

with $\hat{\boldsymbol{M}} = \boldsymbol{P}(\boldsymbol{\Psi} \otimes \boldsymbol{\Psi}^*)\boldsymbol{P}^{-1}$, where $\otimes$ is the Kronecker product and $\boldsymbol{P}$ is a 4×4 matrix derived from Pauli matrices[2]. The depolarization power is obtained from the Müller matrix, $D = 1 - \sqrt{[\mathrm{tr}(\boldsymbol{M}^{\mathrm{T}}\boldsymbol{M}) - {\mathrm{m}_{00}}^2]/(3{\mathrm{m}_{00}}^2)}$, where m_{00} is the first Müller matrix element[1].
The DOP is associated with one positive-semidefinite quadratic form using a single Stokes vector, while D is associated with the average of 12 positive-semidefinite quadratic forms of 6 Stokes vectors[1]. Indeed, one can show that D is similar to the average between $\Delta = 1 - \mathrm{DOP}$ for horizontal (Δ_Q), 45-deg (Δ_U) and circular (Δ_V) input states, which is confirmed in **Figure 3a**. This makes D a robust and unambiguous measure of depolarization but only provides the average of the principle depolarization factors. Thus, depolarization power does not offer the maximum detection sensitivity to visualize GNRs.

The decomposition of the Müller matrix has been an important topic in polarimetry calculus[4]. Using polar decomposition, any Müller matrix can be decomposed into three factors: a diattenuator ($\boldsymbol{M_\mu}$), followed by a retarder ($\boldsymbol{M_R}$), then followed by a depolarizing element ($\boldsymbol{M_\Delta}$). This decomposition is of particular importance as it separates the depolarizing component ($\boldsymbol{M_\Delta}$) from the non-depolarizing $\boldsymbol{M_R}$, $\boldsymbol{M_\mu}$. It should be noted that the diattenuating component ($\boldsymbol{M_\mu}$) describes bulk diattenuation, not variance of diattenuation. The variance of the diattenuation causing depolarization is included in $\boldsymbol{M_\Delta}$. Although different decomposition orders can be envisioned, we chose to have the depolarizing component following the non-depolarizing components during decomposition, $\boldsymbol{M} = \boldsymbol{M_\Delta M_R M_\mu}$. This decomposition was applied to remove the diattenuating and retarding factor from the reconstructed Müller matrix and obtain a pure depolarizer. For completeness, here we present a brief derivation of the polar decomposition.
Our derivation closely follows Lu and Chipman[4]. The diattenuation factor is given by

$$\boldsymbol{M_\mu} = m_{00} \begin{bmatrix} 1 & \overrightarrow{\mu}^{\mathrm{T}} \\ \overrightarrow{\mu} & \boldsymbol{m_\mu} \end{bmatrix}, \tag{S5}$$

where $\overrightarrow{\mu} = 1/m_{00}[m_{01}\ m_{02}\ n_{03}]^{\mathrm{T}}$ is the diattenuation vector consisting of the first row of the measured Müller matrix and $\boldsymbol{m_\mu} = \sqrt{1-\mu^2}\boldsymbol{I} + (1-\sqrt{1-\mu^2})\hat{\mu}\hat{\mu}^{\mathrm{T}}$ is a submatrix where $\boldsymbol{I}$ is the 3×3 identity matrix, $\hat{\mu} = \overrightarrow{\mu}/|\overrightarrow{\mu}|$ denotes the unit vector along $\overrightarrow{\mu}$ and $\mu = |\overrightarrow{\mu}|$. After removing the diattenuating factor, $\boldsymbol{M'} = \boldsymbol{M}{\boldsymbol{M_\mu}}^{-1}$, the remaining matrix contains both retardance and depolarization,

$$\begin{aligned} \boldsymbol{M'} = \boldsymbol{M_\Delta M_R} &= \begin{bmatrix} 1 & \overrightarrow{0}^{\mathrm{T}} \\ \overrightarrow{P_\Delta} & \boldsymbol{m'} \end{bmatrix} \\ &= \begin{bmatrix} 1 & \overrightarrow{0}^{\mathrm{T}} \\ \overrightarrow{P_\Delta} & \boldsymbol{m_\Delta m_R} \end{bmatrix}, \end{aligned} \tag{S6}$$

where $\overrightarrow{P_\Delta} = (\overrightarrow{P} - \boldsymbol{m}\overrightarrow{\mu})/(1-\mu^2)$ denotes the polarizance vector of the depolarizer and $\boldsymbol{m}$ is the lower right 3×3 submatrix of the measured Müller matrix $\boldsymbol{M}[2:4, 2:4]$. The 3×3 symmetric submatrix $\boldsymbol{m_\Delta} = {\boldsymbol{m_\Delta}}^{\mathrm{T}}$ can be obtained from the eigenvalues, $v_{1,2,3}$, of the submatrix $\boldsymbol{m'}(\boldsymbol{m'})^{\mathrm{T}}$ as

$$\begin{aligned} \boldsymbol{m_\Delta} = \pm \left[\boldsymbol{m'}(\boldsymbol{m'})^{\mathrm{T}} + (\sqrt{v_1 v_2} + \sqrt{v_2 v_3} + \sqrt{v_3 v_1})\,\boldsymbol{I}\right]^{-1} \times \\ \left[(\sqrt{v_1} + \sqrt{v_2} + \sqrt{v_3})\,\boldsymbol{m'}(\boldsymbol{m'})^{\mathrm{T}} + \sqrt{v_1 v_2 v_3}\boldsymbol{I}\right] \end{aligned} \tag{S7}$$

If $\det(\boldsymbol{m'}) < 0$ then the minus sign is applied, otherwise the plus sign is used. The most general form for a pure depolarizer can now be written as

$$\boldsymbol{M_\Delta} = \begin{bmatrix} 1 & \overrightarrow{0} \\ \overrightarrow{P_\Delta} & \boldsymbol{m_\Delta} \end{bmatrix}. \tag{S8}$$

This depolarizer has 9 degrees of freedom and has zero diattenuation or retardance. The polarizance character-

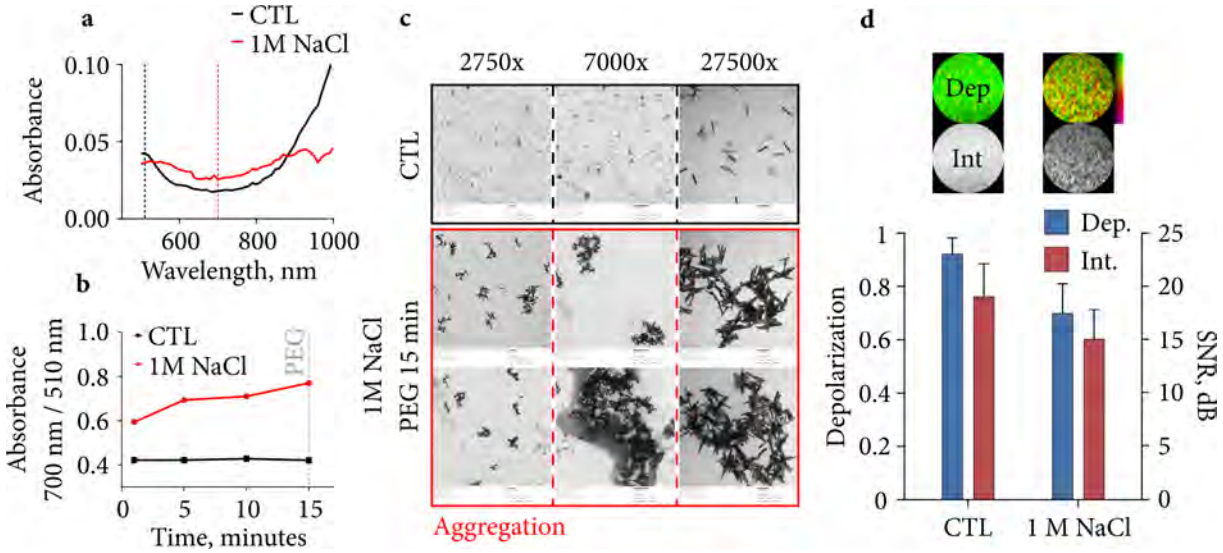

Figure S3 | GNR aggregation. a, Absorbance spectrum analysis of NaCl-mediated GNR aggregation, compared with a non-aggregated control sample. **b**, Aggregation index using the absorbance ratio at 700 nm (red line in **a**) and 510 nm (black line in **a**). GNR aggregation was stopped by applying PEG after 15 minutes. **c**, Electron microscope images at different magnifications of control GNRs (black) and aggregated GNRs (red). **d**, Measured depolarization and backscattering intensity for control GNRs and aggregates. GNR concentration was 400 pM (2.4×10^{11} GNRs/mL). Colour bar represents depolarization, 0 - 1.

izes the polarising capability of the depolarizer, while the eigenvalues and eigenvectors of the 3 × 3 submatrix $\boldsymbol{m_\Delta}$ characterize depolarization properties. The eigenvectors define three (orthogonal) principle axes. The smallest of three corresponding eigenvalues, $v_\Delta^{\min}$, is selected, which points to the principle axis inflicting strongest depolarization, visualized as $\Delta = 1 - v_\Delta^{\min}$ for display. All measurements seen in **Figure 4 - 6** and **Supplementary Figure S4**, **S5**, **S8 - S10** were obtained applying polar decomposition to display definitive depolarization.

III. GOLD NANOROD AGGREGATION

Aggregation of nanoparticles[5] is a common problem and impairs many modalities for GNR detection, including surface enhanced Raman scattering (SERS), two-photon luminescence (TPL) microscopy, dark-field microscopy, photothermal imaging and spectroscopic analysis. Aggregation can shift or reduce plasmon resonance peaks, and compromises the sensitivity of these techniques. To evaluate the impact of GNR aggregation on the depolarization signal, we used NaCl-mediated aggregation of GNRs, confirmed by UV-Vis absorbance spectrum analysis (**Supplementary Figure S3a**). Absorbance measurements were limited to a wavelength of 1000 nm and could not resolve the longitudinal SPR at 1200 nm entirely. Aggregates show a decrease in both peaks at 510 nm and 1000 nm and an overall increase in absorbance between the peaks. SPR dependent techniques such as SERS and differential analysis are likely to yield no or very poor contrast in such conditions. The ratio of sample absorbance at 700 nm and 510 nm served as a measure of aggregation (**Supplementary Figure S3b**), which was further confirmed by electron microscopy (**Supplementary Figure S3c**). Highly aggregated GNRs show a decrease in both depolarization and scattering (**Supplementary Figure S3d**). While the quantitative evaluation of GNR concentration would suffer under these conditions, a qualitative detection of aggregated GNRs by means of their depolarization signature remains possible. This suggests that depolarization, which depends on the GNR differential cross-section, may be more robust to GNR aggregation than techniques that rely on a specific SPR.

IV. ANALYTICAL MODEL

The ability to recover absolute concentration would be extremely enabling for nanoparticle metrology. As seen in the simulation in **Figure 3c**, polarization-maintaining scattering biases a depolarization measurement and makes reconstruction of the highly desirable GNR concentration challenging. When GNRs are injected into biological tissue, susceptibility to polarization-maintaining scattering cannot be ignored. This is confirmed experimentally by utilizing GNRs mixed with non-depolarizing solutions (**Figure 6a**). The backscattering intensity increases with increasing intralipid (IL) concentration as the total number of scatterers increases. Furthermore, the gradient between the backscattering intensity and GNR concentration decreases for increasing non-depolarizing scatterers because the

scattering from GNRs becomes negligible compared to non-depolarizing particles. Depolarization and intensity have a mutual correlation with the number of depolarizing and polarization-maintaining scatterers, and both are measurable quantities. The total backscattering intensity and attenuation coefficient is proportional to the number of total scatterers, $I \propto N_D + N_{ND}$, where N_D is the number of depolarizing particles (GNRs) and N_{ND} is the number of non-depolarizing particles. To describe the recovered depolarization as a function of N_D and N_{ND}, we have identified a simple analytical model,

$$\Delta_{\max} = \mu \left[1 - \exp\left(-\frac{N_D}{N_{ND}} \right) \right], \tag{S9}$$

where μ is the diattenuation of a GNR. Notice that Equation S9 offers maximum depolarization, as is given by the GNR diattenuation coefficient at a circular input state. Moreover, it is equivalent to the depolarization at the object's optimum principle axis at eigenvalue $\upsilon_{\Delta}^{\min}$ described in **Supplementary Section II**, $\Delta_{\max} = \Delta_{\mathrm{V}} = 1 - \upsilon_{\Delta}^{\min}$. Substituting back into Equation S9 and normalizing to the measured intensity, I_{ref}, of a known GNR concentration, M_{ref} (in Molar), we eliminate the unknown non-depolarizing factor and solve for GNR concentration as

$$N_D = \frac{-\ln\left(1 - \frac{\Delta}{\mu}\right) I}{1 - \ln\left(1 - \frac{\Delta}{\mu}\right)} \frac{M_{\mathrm{ref}}}{I_{\mathrm{ref}}} \frac{N_A}{1000} \quad [\mathrm{GNRs/mL}], \tag{S10}$$

where N_A is Avogadro's constant. The analytical model is in good agreement with the numerical model used in the simulations apart from a marginal overestimation for concentrations smaller than 6×10^9 GNRs/mL (10 pM) (**Figure 6b**).

V. COMPARISON – FLUORESCENCE AND TWO-PHOTON LUMINESCENCE

In order to compare depolarization imaging with existing strategies to visualize GNRs, we performed two-photon luminescence (TPL) microscopy and confocal imaging of fluorescently labelled GNRs. To assess the dynamic range and the detection limit, we measured a wide range of GNR concentrations. In addition we qualitatively compared depolarization and fluorescence imaging of organoids incubated with fluorescently labelled GNRs.

GNRs with an SPR at 1200 nm were labelled with AlexaFluor594 (see **Methods**) as a fluorescent marker[6]. TPL was excited at 1000 nm in GNRs with an SPR at 1060 nm (see **Methods**). GNRs were diluted over a wide range of concentrations using phosphate-buffered saline (PBS). For the fluorescence and TPL measurements, the incident optical power was adjusted so that the signal from the highest concentration was close to detector saturation, which is in accord with tissue imaging. Comparison to the concentration at the detection limit (SNR = 1) with the same detector setting indicates the dynamic range. The top inset in **Supplementary Figure S4a** shows GNR absorbance. The green and orange lines indicate fluorescence excitation and emission (detection) that were intentionally chosen to lie between the two GNR resonance peaks for maximum efficiency. The lower inset in **Supplementary Figure S4a** shows the TPL signal, indicating a square relationship with pump power, thus identifying the detected signal as two-photon luminescence. TPL spanned the range from 3×10^9 GNRs/mL (6 pM) to 4×10^{11} GNRs/mL (0.6 nM), yielding two orders of magnitude (21 dB) of measurable GNR concentration (**Supplementary Figure S4a**, green points). The fluorescence signal spanned 28 dB of measurable GNR concentration (from 2.4×10^9 GNRs/mL to 1.8×10^{12} GNRs/mL, 4 pM to 3 nM) (**Supplementary Figure S4a**, blue points). Different photomultiplier tubes used for fluorescence and TPL detection had slightly different saturation thresholds. Interestingly, two independent preparations of GNR labelling used subsequently for the concentrations from 4 - 400 pM and 1 - 3 nM, respectively, led to an inconsistency in the fluorescence curve at a concentration of 3×10^{11} GNRs/mL (500 pM) (blue, dashed circle), effectively leading to an overestimation of the dynamic range. This illustrates one of the difficulties in deriving GNR concentration from calibrated fluorescence measurements. The inset in **Supplementary Figure S4b** shows the corresponding depolarization. The measured depolarization and scattering intensity was used to calculate absolute GNR concentration (**Supplementary Figure S4b**) using the analytical model described in **Supplementary Section IV** (Equation S9, S10). Depolarization measurements do not show an inconsistency as seen by fluorescence because depolarization is directly dependent on GNR concentration and not conjugated fluorescent molecules. The detection dynamic range and detection limit of the GNR depolarization signature are comparable with those of fluorescent detection, albeit without being subject to experimental inaccuracies in the preparation of labelled GNRs. Importantly, depolarization does not suffer from photobleaching, which is the main obstacle in obtaining reliable measurements from fluorescence. However, confocal and TPL microscopy can offer higher spatial resolution, and adapting the detector setting enables single molecule detection. Depolarization, in contrast, requires and ensemble of GNRs. Future investigation on single particle diattenuation could provide an interesting mechanism to mitigate against this current limitation.

Fluorescent GNRs were added to PFA-fixed cerebral organoids prepared according to a previously published protocol[7]. Cerebral organoids were incubated with GNRs for 1 hour. **Supplementary Figure S4c** shows scattering intensity and depolarization images. Depolarizing areas well beyond 800 µm can be identified,

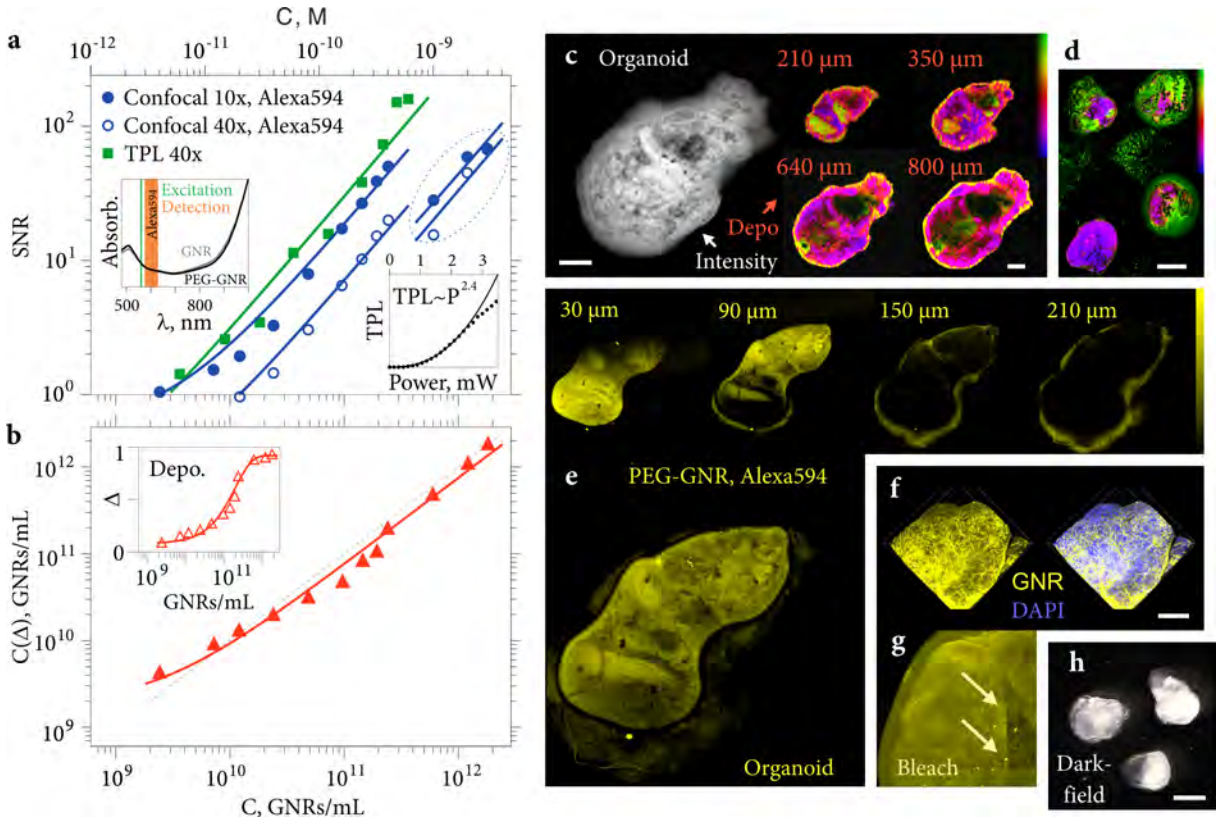

Figure S4 | Comparison with fluorescence and two-photon luminescence. a, Confocal detection of fluorescent GNRs (blue points) and two-photon luminescence (TPL, green points) signal for different GNR concentrations. The top inset shows absorbance of GNRs with SPRs at 510 nm and 1200 nm. The green line indicates the fluorescence excitation wavelength (559 nm). The orange area illustrates the bandpass filter for fluorescence emission / detection (575 - 620 nm). The lower inset illustrates a square relationship between TPL signal and input power, identifying the signal as two-photon luminescence. Lines represent linear fits. **b**, Measured GNR concentrations for different set GNR concentrations using the depolarization signature and analytic model. The measured depolarization (Δ) is shown in the inset. Black, dashed line indicates expected concentrations and red line shows linear fit. **c**, Volumetric intensity projection and depth-sectioned depolarization images of a cerebral organoid incubated with PEG-GNRs. **d**, Volumetric depolarization projection showing a wide field of view of four cerebral organoids incubated with GNRs, acquired in 10 seconds. **e**, Depth-sectioned images of fluorescent GNRs in a similar cerebral organoid using an inverted confocal microscope. **f**, Overlay of GNR fluorescence and DAPI. **g**, Example of photobleaching of fluorescence. **h**, Dark-field microscope image of three cerebral organoids. Colour bar represents depolarization, 0 - 1 (**c**, **d**), relative fluorescence intensity (**e**). Scale bars, 200 µm (**c**, **f**), 1 mm (**d**), 2 mm (**h**).

with maximum imaging depths of 1.5 mm (**Figure 4**,**5**). For demonstration purposes, **Supplementary Figure S4d** shows a wide field of view volumetric-projection of 4 cerebral organoids that was acquired in 10 seconds, evidencing the high imaging speed warranted by depolarization. A comparison with confocal imaging of fluorescent GNRs confirms the presence of GNRs in the organoids, but discloses the detection of only minimal fluorescence beyond 150 µm depth (**Supplementary Figure S4e**). Fluorescence imaging of DAPI-stained organoids reveals GNR accumulation predominantly in the interstitial space between the cells (**Supplementary Figure S4f**). Multiplexing with a GNR depolarization signature may be possible. Depolarization by GNRs is tunable with GNR aspect ratio and easily exceeds wavelength limitations of fluorescent probes, proteins or dyes. **Supplementary Figure S4g** illustrates an example of photobleaching that occurred by previously imaging a particular region of interest, which undermines the assessment of absolute GNR concentration with fluorescence. For completeness, **Supplementary Figure S4h** shows a dark-field image of selected cerebral organoids to appreciate a 2D structural visualization in the visible spectral region.

Signal-to-noise-ratio limitations

The fluorescence signal is directly proportional to concentration (GNRs, fluorophores) and excitation power, and is decreased by any loss in the excitation or emission pathways. The fluorescence signal in a homogenous sample is thus affected by scattering and absorption (Beer-Lambert's law) and exponentially decreases with depth, even if the GNR concentration remains constant. The same applies for TPL and

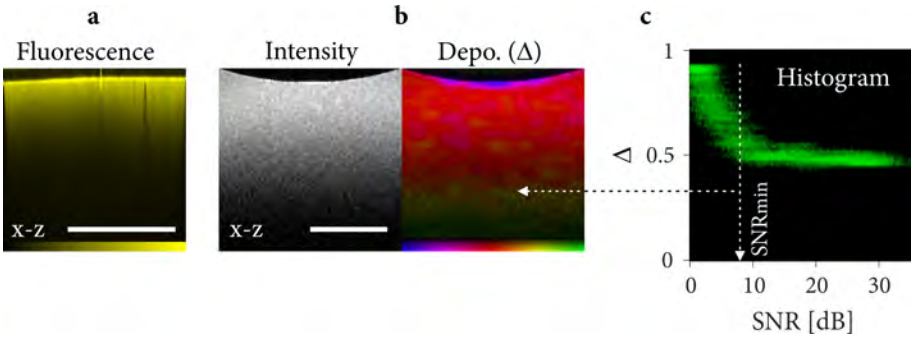

Figure S5 | Noise limitations. a, Depth-resolved fluorescence of 1 nM GNRs mixed with intralipid, imaged with confocal microscopy. The fluorescence signal decreases along depth due to sample attenuation. **b**, Backscattering intensity and depolarization of the identical sample in (**a**). Depolarization remains constant and independent of sample attenuation over a wide range of SNR. **c**, 2D histogram of depolarization and SNR. Depolarization remains constant above a SNR of 8 dB. Lower SNR is increasingly biased due to randomly polarized background noise. Colour bars represent relative fluorescence signal (**a**), depolarization, 0 - 1 (**b**). Scale bars, 500 μm (**a**), 1 mm (**b**).

spectroscopic (differential scattering) approaches. An example of this depth-dependent signal drop can be seen in **Supplementary Figure S5a** showing fluorescent GNRs (1 nM) mixed with intralipid (0.5 % w/w) to mimic turbid media. **Supplementary Figure S5b** displays the backscattering intensity that features a similar signal decay due to scattering and absorption, although the longer wavelength employed for coherent imaging reduces the effective attenuation and increases imaging depth. In comparison, the depolarization from GNRs, shown in **Supplementary Figure S5b**, remains remarkably constant for a fixed GNR concentration, independent of imaging depth and sample attenuation, above a minimum signal-to-noise ratio (SNR). At low SNR, the signal becomes dominated by noise, which is randomly polarized and biases the measurement toward increased depolarization. This is illustrated with a 2D histogram, reporting the measured depolarization at a given SNR, suggesting that the depolarization bias from noise cannot be ignored below a SNR of 8 dB (white dashed line) (**Supplementary Figure S5c**). To avoid this bias, measurements with a SNR below 8 dB were masked throughout this study. However, above this threshold, depolarization provides a quantitative metric that is largely independent of the underlying scattering strength.

VI. SIGNIFICANCE

The depolarization signature from gold nanorods (GNRs) could find many applications: (1) the use of GNRs as a contrast agent, which would require formulation of highly biocompatible materials, (2) the use of GNRs as a "nano-scale beacon" to label larger materials such as polymer nanoparticles, DNA origami or liposomes to monitor their tissue accumulation, and (3) the use of GNRs as a "universal carrier" for drugs, biological therapeutics, etc.

Great progress in whole body imaging modalities now allows the observation of biological processes and effects of pharmacological substances, including bioluminescence detection[8,9] and photothermal detection. Their resolution is on the hundreds of micrometre to millimetre scale with modest acquisition times, offering macroscopic details and often asking for subject immobilization. While readily implemented, these approaches have no depth-resolving (3D) capability. Opto / photoacoustic imaging (tomography) has recently become available as a deep tissue imaging modality and could provide an inexpensive replacement for whole (small) animal imaging in 3D, at fast speeds and a modest resolution of several hundreds of micrometers[10,11].

Resolving micrometre sized vessels and tumours would be highly enabling for early stage diagnostic, therapeutic purposes and pre-clinical anatomical models. Confocal, two- or multiphoton techniques can offer close to diffraction limited resolution and are well suited for molecular imaging by detection of optical reporters such as fluorescent probes and proteins. Unfortunately, they operate at depths of a few mean free paths (MFP $<$ 100 μm in tissue)[12] with short working distances.

Interferometric techniques provide high resolution depth sectioning while using low NA objective lenses and longer working distances that offer unique clinical abilities. Their easy implementation at wavelengths beyond 1 μm supports reduced scattering and yields imaging depths up to 1 - 2 transport mean free paths (TMFP $\sim$ 10 MFP, 1 - 2 mm) with 2 - 6 μm axial resolution in tissue.

While powerful and rich in application, the excitation and emission of fluorescence has drawbacks, including autofluorescence, quenching[6], photobleaching and the general inability to operate in the low scattering (high penetration) near-infrared spectral region ($>$ 800 nm). Quenching, photobleaching, absorbance and photomultiplier tube nonlinearities make the quantitation of (nanoparticle) concentration ambiguous and difficult,

only allowing a qualitative visualization.

Depolarization is an instantaneous process, allows fast acquisition and does not suffer from photobleaching, quenching or autofluorescence. Measuring depolarization does not require a pulsed laser or additional light sources and photon densities within safety limits of the human eye are sufficient. Depolarization offers an absolute measure of GNR concentration that could inspire new research of GNRs as a carrier for drugs and antibodies or as nano-scale beacon for larger objects. Because depolarization arises from elastic scattering, it is particularly well suited for linear microscopy and avoids the need of femtosecond pulses and high photon densities from mode-locked lasers. Depolarization allows GNR detection across a large wavelength span, tunable by the SPR wavelength. The access to longer wavelength (beyond typical fluorescence and two-photon wavelengths) reduces scattering and increases imaging depth. The identification of diattenuation as the underlying source of GNR depolarization (**Supplementary Section I**) allows simple numerical simulations of measured depolarization under different scenarios, in comparison to fluorescence or nonlinear processes. GNR depolarization could allow coherent ranging techniques to gain molecular specificity. Labelling with GNRs may have more limitations than fluorescent labelling, but offers quantitative concentration measurements. Finally, the concept of GNR depolarization and diattenuation may be adaptable to other microscopy techniques, including confocal and dark-field microscopy.

[1] Gil, J.J., Bernabeu, E. Depolarization and polarization indices of an optical system. *Optica Acta* **33**(2), 185 – 189 (1986).

[2] Kim, K., Mandel, L., Wolf, E. Relationship between Jones and Mueller matrices for random media. *J. Opt. Soc. Am. A* **4**(3), 433 – 437 (1987).

[3] Simon, B.N. et al. A complete characterization of pre-Mueller and Mueller matrices in polarization optics. *J. Opt. Soc. Am. A-Opt. Image Sci. Vis.* **27**, 188 – 199 (2010).

[4] Lu, S., Chipman, R.A. Interpretation of Mueller matrices based on polar decomposition. *J. Opt. Soc. Am. A* **13**(5), 1106 – 1113 (1996).

[5] Albanese, A., Chan, W.C.W. Effect of gold nanoparticle aggregation on cell uptake and toxicity. *ACS Nano* **5**, 5478 – 5489 (2011).

[6] Chou, L.Y.T., Chan, W.C.W. Fluorescence-Tagged Gold Nanoparticles for Rapidly Characterizing the Size-Dependent Biodistribution in Tumor Models. *Adv. Healthc. Mater.* **1**, 714 – 721 (2012).

[7] Lancaster, M.A. et al. Cerebral organoids model human brain development and microcephaly. *Nature* **501**, 373 – 379 (2013).

[8] Prescher, J.A., Contag, C.H. Guided by the light: visualizing biomolecular processes in living animals with bioluminescence. *Curr. Opin. Chem. Biol.* **14**(1), 80 – 89 (2010).

[9] Evans, M.S. et al. A synthetic luciferin improves bioluminescence imaging in live mice. *Nature Methods* **11**, 393 – 395 (2014).

[10] Razansky, D. et al. Multispectral opto-acoustic tomography of deep-seated fluorescent proteins in vivo. *Nature Photonics* **3**, 412 – 417 (2009).

[11] Merĉep, E., Burton, N.C., Claussen, J., Razansky, D. Whole-body live mouse imaging by hybrid reflection-mode ultrasound and optoacoustic tomography. *Opt. Lett.* **40**(20), 4643 – 4646 (2015).

[12] Ntziachristos, V. Going deeper than microscopy: the optical imaging frontier in biology. *Nature Methods* **7**(8), 603 – 614 (2010).

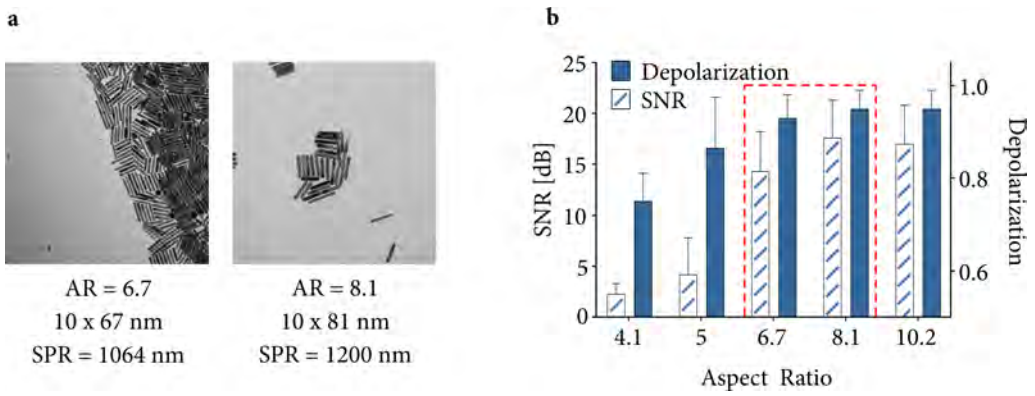

Figure S6 | Gold nanorods. a, Electron microscope images of GNRs used for experiments with an aspect ratio of 6.7 and 8.1 and a surface plasmon resonance at 1064 nm and 1200 nm, respectively. **b**, Measured backscattering intensity and depolarization of GNRs of different aspect ratios at a wavelength of 1.3 µm. The red box marks GNRs used for experiments.

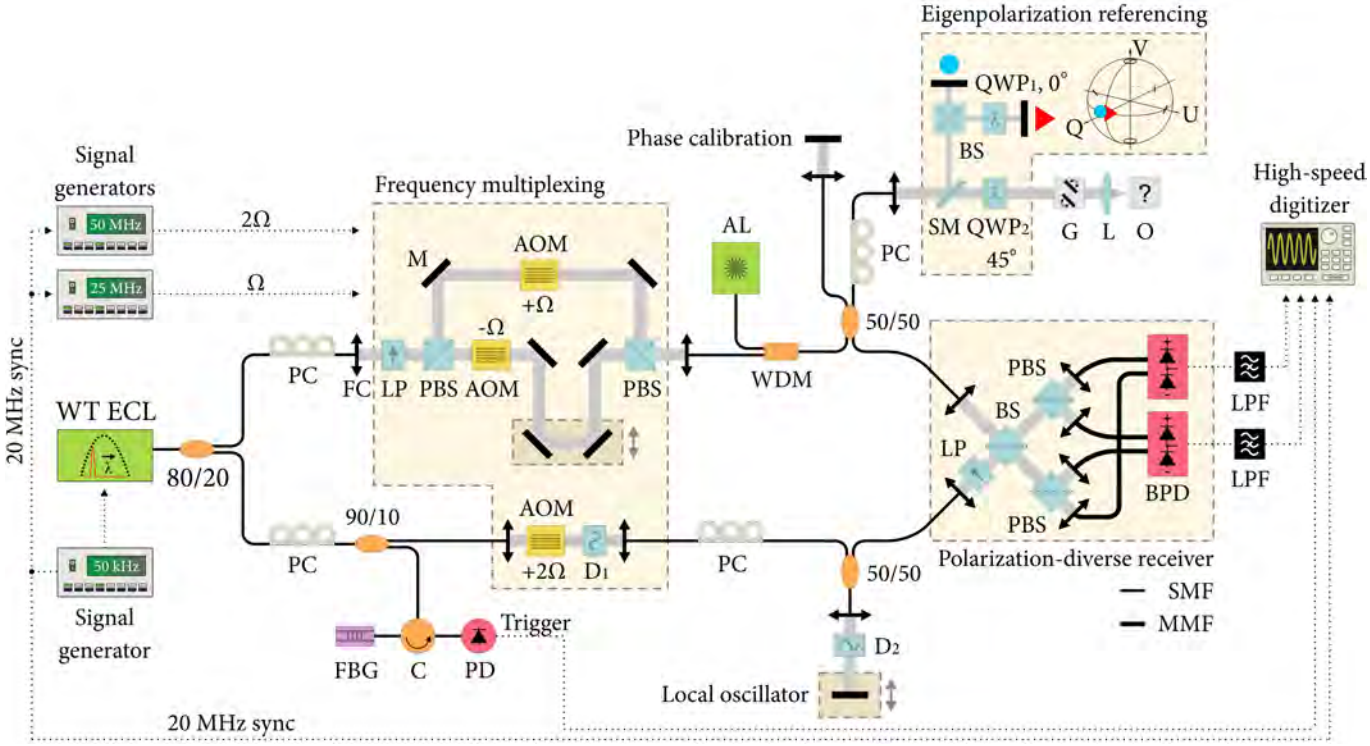

Figure S7 | Experimental set-up. Polarimetry and three-dimensional microscopy was performed in an optical frequency domain imaging setting (also known as coherent frequency-domain reflectometry). The 34 GHz linewidth of a custom built wavelength tunable external cavity laser (WT ECL) was swept at 50 kHz across a 20 THz optical bandwidth, centred at 1.3 µm. A set of basis vectors (two orthogonal states in Jones space) were incident at the object simultaneously. A combination of acoustic optical modulators (AOM) enabled demodulation of the depth signals of each polarization state, centred about two beating frequencies ($2\Omega \pm \Omega$) after heterodyne detection. A polarization diverse detection ensemble casts the Jones vector and Jones matrix. Polarization controller (PC), fibre collimator (FC), linear polarizer (LP), polarizing beam splitter (PBS), mirror (M), aiming laser (AL), wavelength division multiplexing (WDM), lens (L), semi-transparent mirror (SM), quarter-wave plate (QWP), galvanometer mirror (G), object (O), 50/50 beam splitter (BS), fibre Bragg grating (FBG), circulator (C), photodiode (PD), chromatic dispersion compensating material (D), balanced photodiode (BPD), low-pass filter (LPF), single-mode fibre (SMF), multi-mode fibre (MMF).

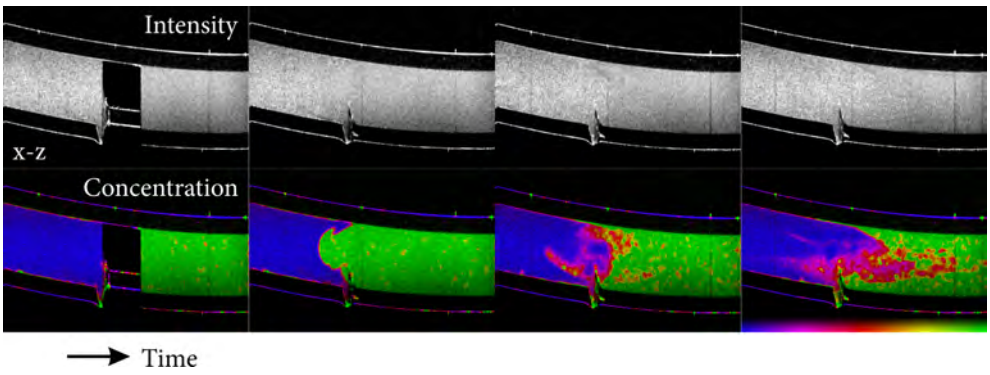

Figure S8 | Gold nanorod concentration. Depth-resolved (x-z) view of GNR concentration during mixing with a non-depolarizing (IL) solution. Colour bar represents GNR concentration, 0 - 2.4×10^{11} GNRs/mL (0 - 400 pM).

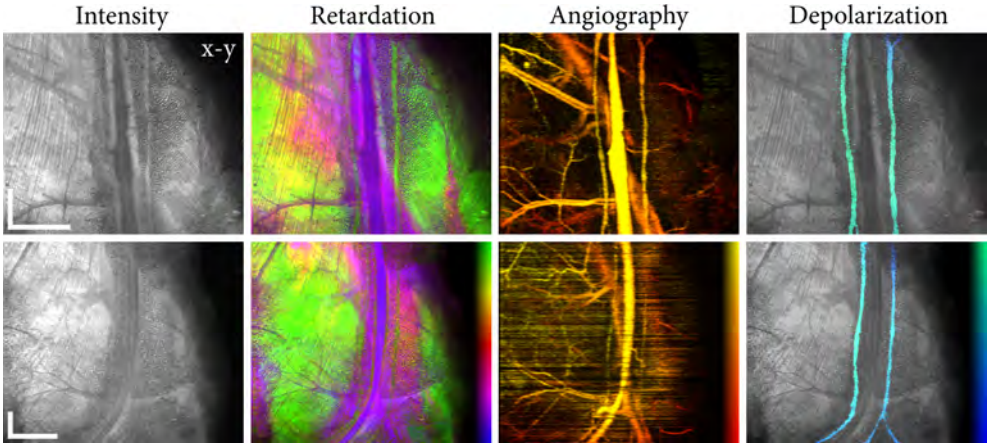

Figure S9 | Mouse lymph vessel *in vivo*. Volumetric projections (x-y) of mice lymphatic vessels after injecting 10 µL of 38 nM gold nanorods into the foot. Intensity, local retardation, angiography, and depolarization contrast is shown. The angiogram shows superficial vessels in yellow and deeper vessels in red. Depolarization is encoded in depth where bright blue represents superficial and dark blue deeper regions of depolarization. Angiography can detect GNRs in the lymphatic vessel, but motion artefacts (e.g. heartbeat, breathing, etc.) often disturb angiograms as seen in the lower row. Scale bars, 2 mm.

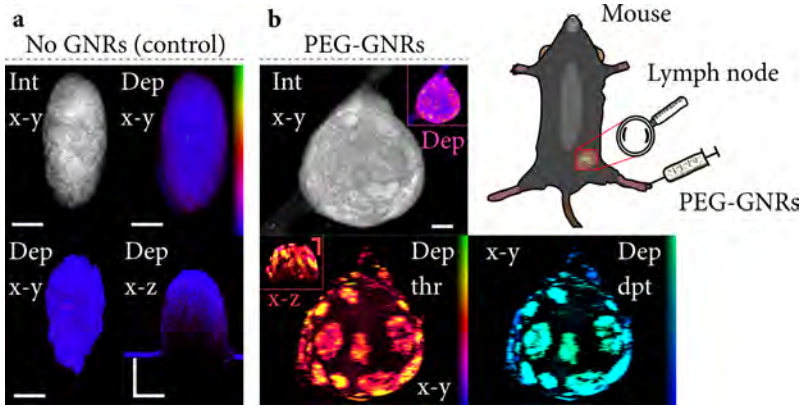

Figure S10 | Gold nanorod transport in mouse lymph node. a, Control measurement of a lymph node showing volumetric projections (x-y) of intensity and depolarization (top row), depolarization in a depth-resolved (x-y) view at a depth of 290 µm (bottom left) and a x-z depth-resolved view (bottom right). **b**, Depth projections (x-y) of the volumetric data of an excised lymph node 72 hours postinjection of three times 15 µL of 35 nM PEG-GNRs over the course of 48 hours. The top shows intensity and the bottom depolarization (> 0.2). Top inset shows the depolarization without threshold. Lower inset shows depolarization in x-z direction. The bottom right image (Dep dpt) shows depth-encoded depolarization, displaying superficial regions as bright blue and deeper regions of depolarization as dark blue. Depth span, 1.2 mm. Scale bars, 500 µm.